Stress Intensity Factor Gauging by Digital Image Correlation: Application in Cyclic Fatigue

Rami Hamam, François Hild, Stéphane Roux

Submitted to *Strain*, July 2006, revised October 2006

STRESS INTENSITY FACTOR GAUGING BY DIGITAL IMAGE CORRELATION: APPLICATION IN CYCLIC FATIGUE

Rami HAMAM[1], François HILD[1,*] and Stéphane ROUX,[2]

[1]*LMT-Cachan, ENS-Cachan / CNRS UMR 8535 / Université Paris 6*

61 avenue du Président Wilson, F-94235 Cachan Cedex, France

[2]*Laboratoire Surface du Verre et Interfaces, UMR 125 CNRS / Saint Gobain*

39 quai Lucien Lefranc, F-93303 Aubervilliers Cedex, France

Running head title: SIF gauging by DIC in fatigue

[*]Corresponding author: Fax: +33 1 47 40 22 40, Email: hild@lmt.ens-cachan.fr

STRESS INTENSITY FACTOR GAUGING BY DIGITAL IMAGE CORRELATION: APPLICATION IN CYCLIC FATIGUE

by

Rami HAMAM, François HILD and Stéphane ROUX

Abstract:

A fatigue crack in steel (CCT geometry) is studied via digital image correlation. The measurement of the stress intensity factor change during one cycle is performed using a decomposition of the displacement field onto a tailored set of elastic fields. The same analysis is performed using two different routes, namely, the first one consists in computing the displacement field using a general correlation technique providing the displacement field projected onto finite element shape functions, and then analysing this displacement field in terms of the selected mechanically relevant fields. The second strategy, called integrated approach, directly estimates the amplitude of these elastic fields from the correlation of successive images. Both procedures give consistent results, and offer very good performances in the evaluation of the crack tip position (uncertainty of about 20 μm for a 14.5-mm crack), stress intensity factors (uncertainty less than $1\,\mathrm{MPa}\sqrt{\mathrm{m}}$) and opening properties.

Keywords:

Correlation algorithm, crack opening, identification technique, integrated approach, Photomechanics.

1. Introduction

One of the commonly encountered mechanical failures is fracture dominated. It usually occurs before large scale yielding. In many materials, small scale yielding arises in the vicinity of the crack tip. Therefore, the classical elastic solutions [1] are only first order idealizations of the practical situation. Elastic-Plastic Fracture Mechanics (EPFM) aims at analysing more complex situations for which plasticity needs to be accounted for with global quantities. Other routes are also developed following local approaches to fracture [2]. They are not discussed herein.

Different quantities are introduced to describe cracks in a small scale yielding regime. The crack opening displacement was proposed as a fracture parameter to analyze propagation under quasi-static [3] and cyclic [4] loading conditions. However, the critical values of crack opening displacements were not always easy to evaluate. Rice [5] considered the potential energy changes induced by crack growth in a non-linear elastic material. This author introduced a path-independent contour integral, the *J*-integral. It is used to predict the inception of crack propagation. The so-called HRR fields [6,7] were also introduced to describe more locally the stress and strain fields in non-linear elastic materials.

With the development of full-field measurement techniques, some of the aspects discussed above are assessed experimentally with or without having to use numerical simulations. Under these circumstances, the measurable quantities are usually displacement fields [8]. Among various techniques, Digital Image Correlation (DIC) has already been applied to analyze cracks in homogeneous and heterogeneous materials [9]. Least squares techniques are used to post-process displacement fields to extract stress intensity factors by using one or more elastic fields [10,11]. This simple extraction method will be used herein. An alternative technique to determine stress intensity factors is to evaluate directly the *J*-integral along a given contour [12] or an interaction integral [13] to use more measurement

points. By measuring crack opening displacements, stress intensity factors are evaluated for brittle materials [14] and crack closure was studied in fatigue [15] by using a long-distance microscope. In the present case, stress intensity factors will be used to analyse opening properties in fatigue.

In this paper, it is proposed to introduce an enriched crack kinematics in cyclic fatigue by using two types of DIC techniques applied to the measurement of stress intensity factors. It generalizes the approaches proposed by the authors [16] to account for non-linear effects close to the crack tip. It can be noted that more local quantities (e.g., near-tip displacements [17]) are also used to analyse crack opening/closure. Section 2 is devoted to the presentation of a new enriched crack kinematics in small scale yielding to avoid numerical simulations [17] or to use HRR fields [13]. It is based upon "supersingular" and subsingular displacement fields. The first supersingular field is used to evaluate the crack tip position as opposed to the method that consists in considering the position as one of the minimisation parameters [10,11]. In Section 3, an *a posteriori* identification technique allows for the analysis of one loading/unloading cycle by using supersingular and subsingular displacement fields. An *integrated* approach is presented in Section 4. It consists in a *coupled* and *a priori* way of dealing with measurement *and* identification [16]. In both cases, the opening load is determined from the stress intensity factor history.

2. Enriched crack kinematics

Linear Elastic Fracture Mechanics (LEFM) has proven to capture the most salient features of fracture, in spite of the fact that it is based on an elastic description of the solid. The reason for this success is the fact that the elastic singular crack field captures the mechanical behaviour outside the confined crack tip zone where non-linear processes (e.g., plasticity, damage) are taking place [1]. As such, it allows one to bridge the far-field (possibly complicated) elastic loading to the local crack tip through few meaningful loading parameters,

namely the stress intensity factors [18]. This type of analysis is applied herein to cyclic fatigue for an elasto-plastic material, where at the level of the stress intensity factors, no major change is expected past the first loading cycle.

To address this question, let us follow the basic philosophy underlying LEFM, namely, outside the confined process zone where plasticity occurs, the mechanical behaviour of many solids remains linear elastic. Moreover, it is through this elastic field that the crack tip "communicates" with the external loading applied to the solid. Thus the approach is based on a characterization of *elastic fields* radiating from the crack tip. To tackle the problem, one cuts out of the studied crack a domain D containing the crack tip process zone, and substitute to it an equivalent loading applied to the boundary ∂D. The elastic field outside D is identical to the elasto-plastic solution of the medium with its initial (i.e., complete) geometry. The difficulty is that the loading on ∂D to be applied is at this stage unknown. At this level of generality, one still proceeds and solves the elastic problem for an *arbitrary* loading. Such a task is easily performed within the framework of plane elasticity resorting to complex potentials [19]. A closed-form solution for the displacements is derived from the Kolossov-Muskhelishvili potentials φ and ψ, holomorph functions of the complex variable $\mathbf{z} = x + iy$

$$2\mu\mathbf{U}(\mathbf{z}) = \kappa\varphi(\mathbf{z}) - \mathbf{z}\overline{\varphi'(\mathbf{z})} - \overline{\psi(\mathbf{z})} \tag{1}$$

where μ is the Lamé shear modulus, κ a dimensionless elastic (or Kolossov) coefficient related to the Poisson's ratio ν according to $(3 - \nu) / (1 + \nu)$ for plane stress conditions or $3 - 4\nu$ for plane strain conditions, and $\mathbf{U} = U_x + iU_y$ the displacement field.

The crack tip is assumed to lie at the origin of the coordinate $\mathbf{z} = \mathbf{0}$, and the crack is the negative real axis, $\Re(\mathbf{z}) < 0$ and $\Im(\mathbf{z}) = 0$. Such a formulation is very convenient for analyzing (semi-)infinite crack geometries since no characteristic scale is involved. This implies that φ and ψ are homogeneous functions of $\mathbf{z}$, i.e., $\mathbf{z}^{\alpha}$. The crack face boundary condition (i.e., traction free) thus remains to be exploited to select all possible solutions. The

fulfilment of the boundary condition for a non-trivial solution immediately selects the exponent α for the two potentials as a half-integer $\alpha = n/2$. Let us treat separately the cases where a displacement discontinuity is involved, i.e., $n = 1 - 2m$, and where the displacement is continuous, i.e., $n = -2m$.

2.1. Eigen modes

Let us postulate the form of the two potentials as $\varphi(\mathbf{z}) = \mathbf{A}\mathbf{z}^{1/2-m}$ and $\psi(\mathbf{z}) = \mathbf{B}\mathbf{z}^{1/2-m}$. For $m = 0$, the standard singular solution is recovered [18]. In the following, the fields that are less singular ($m < 0$), are termed "subsingular" and those such that $m > 0$ are referred to as "supersingular." The traction-free crack faces imply

$$\mathbf{B} = -(1/2 - m)\mathbf{A} + \overline{\mathbf{A}} \tag{2}$$

Thus one has two modes (namely, $\Re(\mathbf{A})$ and $\Im(\mathbf{A})$) for each m exponent. To identify the "modes," one may note that the displacement along the (upper) crack face, $\theta = \pi$ is along the $i\mathbf{A}$ direction, thus mode I is for real $\mathbf{A}$ whereas mode II is associated with a purely imaginary $\mathbf{A}$. Let us introduce the eigenfunctions $\mathbf{\Omega}_n$ for mode I, (resp. $\mathbf{Y}_n$, for mode II), the displacement field obtained for exponent n and $\mathbf{A} = (-1)^m/\sqrt{2\pi}$ (resp. $\mathbf{A} = i(-1)^m/\sqrt{2\pi}$). Thus

$$\mathbf{\Omega}_n = \frac{(-1)^{(1-n)/2}}{2\mu\sqrt{2\pi}} r^{n/2}\left[\kappa\exp\left(i\frac{n}{2}\theta\right) - \frac{n}{2}\exp\left\{i\left(2-\frac{n}{2}\right)\theta\right\} - \left(1-\frac{n}{2}\right)\exp\left\{-i\frac{n}{2}\theta\right\}\right] \tag{3}$$

and

$$\mathbf{Y}_n = \frac{i(-1)^{(1-n)/2}}{2\mu\sqrt{2\pi}} r^{n/2}\left[\kappa\exp\left(i\frac{n}{2}\theta\right) + \frac{n}{2}\exp\left\{i\left(2-\frac{n}{2}\right)\theta\right\} - \left(1+\frac{n}{2}\right)\exp\left\{-i\frac{n}{2}\theta\right\}\right] \tag{4}$$

The standard elastic field corresponds to $n = 1$. The factor $\sqrt{2\pi}$ is introduced to match the usual definitions of the stress intensity factors K_I and K_{II}, which are thus equal respectively to the amplitudes ω_1 and υ_1 associated with the fields $\mathbf{\Omega}_1$ and $\mathbf{Y}_1$.

2.2. Non-Singular solutions

The case of an even exponent $n = -2m$ is considered. The boundary conditions along the crack faces give

$$\mathbf{B} = m\mathbf{A} - \overline{\mathbf{A}} \tag{5}$$

Thus two modes are again encountered (namely, $\Re(\mathbf{A})$ and $\Im(\mathbf{A})$) for each m exponent. The displacement along the upper crack face, $\theta = \pi$, reads

$$2\mu\mathbf{U}(r,\theta=\pi) = (-1)^m(\kappa+1)\mathbf{A}r^{-m} \tag{6}$$

Thus the displacement is along the **A** direction. For a real **A**, (this case shares the same y to $-y$ symmetry as "mode I"), one obtains the "generalized T-stress" mode in polar coordinates (the T-stress is obtained for $n = 2$ (m = –1) [20]), whereas a purely imaginary $i\mathbf{A}$ gives a contribution that follows the same anti-symmetry as mode II (e.g., a rigid body rotation is obtained for $n = 2$ (or $m = -1$)). Conversely, rigid body translations are obtained for $n = 0$.

2.3. Interpretation

Traditionally, the supersingular fields are ignored because their asymptotic behaviour near the crack tip is non-physical (i.e., diverging energy density). However, for the present purpose, since the crack tip process zone is cut out from the domain of analysis, one does not have to reject these solutions. The most general field is thus looked for as

$$\mathbf{U}(\mathbf{z}) = \sum_n \left[\omega_n \mathbf{\Omega}_n(\mathbf{z}) + \upsilon_n \mathbf{Y}_n(\mathbf{z})\right] \tag{7}$$

where ω_n and υ_n are real numbers.

Under pure mode I, the crack opening discontinuity $[\![\mathbf{U}]\!]$ at $x = -r$ is

$$[\![\mathbf{U}]\!] = \frac{i(\kappa+1)}{\mu\sqrt{2\pi}} \sum_{n\ odd} \omega_n r^{n/2} \tag{8}$$

whereas in mode II,

$$[\![\mathbf{U}]\!] = -\frac{(\kappa+1)}{\mu\sqrt{2\pi}} \sum_{n\ odd} \upsilon_n r^{n/2} \tag{9}$$

2.4. Subsingular fields

Let us first note that the status of the fields $\mathbf{\Omega}_n$ and $\mathbf{Y}_n$ is very different for n less than or greater than 1. For $n > 1$, the fields are called here subsingular. They have no impact on the crack tip. Conversely, the attached stress fields increase with the distance to the crack tip. Such functions are thus useful to match the singular fields with the remote geometry, or boundary conditions. However, since their impact on the crack tip process zone is negligible, one does not insist here on the structure of these fields.

All elastic fields that fulfil the crack face boundary conditions (i.e., the traction on this boundary vanishes) are easily obtained. Moreover, they are naturally *ranked*. A basis for such space of elastic fields is constructed from functions that have a power law dependence with the distance r to the crack tip, with exponent α_n for the n-th field. Sorting out these functions with respect to the exponent α_n allows one to rank them according to their far-field influence. Among these fields, one will find the usual mode I and mode II displacement fields. Looking for an enriched description, it suffices to browse through this library of functions and keep only the lowest orders, at a level that will be judged satisfactory. This point will be addressed later on. The result of this analysis is that a description of the crack is completed from the usual stress intensity factors (SIF) description, by a few additional parameters that are the dominant corrections in the elastic field due to the non-linearity occurring in the process zone. In the case of cyclic loading where a small amount of plastic flow at the crack tip is taking place at each cycle, one will see that even for a periodic SIF evolution, these additional "enriched" parameters may follow a non-periodic change, leading to fatigue.

2.5. Equivalent crack tip position

One follows the hierarchy of fields through a differentiation of the fields with respect to the crack tip position along the *x* direction. The above singular solutions $\mathbf{\Omega}_n$ (respectively $\mathbf{Y}_n$) are also obtained from derivatives of Eq. (3) (resp. (4)) along the *x* direction. To establish such a connection, it is useful to first relate consecutive order functions

$$\frac{\partial \mathbf{\Omega}_n}{\partial x} = -(n/2)\mathbf{\Omega}_{n-2} \quad \text{and} \quad \frac{\partial \mathbf{Y}_n}{\partial x} = -(n/2)\mathbf{Y}_{n-2} \tag{10}$$

Since the position $\mathbf{z}$ is counted from the crack tip position, $\mathbf{z}_0$, the derivative of the field with respect to the crack tip position is the opposite of the above expression

$$\frac{\partial \mathbf{\Omega}_n}{\partial x_{crack}} = (n/2)\mathbf{\Omega}_{n-2} \quad \text{and} \quad \frac{\partial \mathbf{Y}_n}{\partial x_{crack}} = (n/2)\mathbf{Y}_{n-2} \tag{11}$$

A simple recurrence thus provides

$$\frac{\partial^n \mathbf{\Omega}_1}{\partial x_{crack}^n} = (-1)^{n+1} \frac{(2n)!}{n!(2n-1)2^{2n}} \mathbf{\Omega}_{1-2n} \quad \text{for} \quad n \geq 1. \tag{12}$$

The same expression holds for the mode II functions.

If one uses the expression of the expansion (7) together with the derivation property that has been above reported, one notes that

$$\omega_1 \mathbf{\Omega}_1 + \omega_{-1} \mathbf{\Omega}_{-1} = \omega_1 \left(\mathbf{\Omega}_1 + 2 \frac{\omega_{-1}}{\omega_1} \frac{\partial \mathbf{\Omega}_1}{\partial x} \right) \tag{13}$$

This expression is seen as a first order Taylor expansion of a usual crack field whose tip would be located at a position r_1, where

$$r_1 = 2 \frac{\omega_{-1}}{\omega_1} \tag{14}$$

It is important to note that since the crack tip vicinity is affected by the plastic flow of the process zone, the exact position of the tip is only obtained from an extrapolation of the far elastic field. An offset in the crack tip position generates essentially an $\mathbf{\Omega}_{-1}$ correction.

Consequently, one *defines* the crack tip position such that $\omega_{-1} = \mathbf{0}$. Once this position is prescribed, one sees that the first non-trivial correction is a quadrupolar term

$$\omega_1 \mathbf{\Omega}_1 + \omega_{-3} \mathbf{\Omega}_{-3} = \omega_1 \left(\mathbf{\Omega}_1 - \frac{1}{2} \frac{8\omega_{-3}}{\omega_1} \frac{\partial^2 \mathbf{\Omega}_1}{\partial x^2} \right) \tag{15}$$

which is here unambiguously defined. Let us also note that the ratio $r_2^2 = -8\dfrac{\omega_{-3}}{\omega_1}$ is interpreted as proportional to the square of the extent of the process zone, r_2.

2.6. Summary of the approach

With the above results, one addresses the analysis of elasto-plastic kinematic fields. First, the core of the process zone has to be defined and omitted from any subsequent analysis. The outside displacement field is then decomposed over the basis of functions $\mathbf{\Omega}_n$ (mode I) and $\mathbf{Y}_n$ (mode II). The effective crack tip position is estimated from the relative importance of the ω_{-1} and ω_1 (or υ_{-1} and υ_1) amplitudes.

3. A posteriori identification of SIFs

3.1. Experimental configuration and kinematic measurements

The studied material is an XC48 (or C45) steel with a Young's modulus of 190 GPa, a Poisson's ratio of 0.3. The cyclic yield stress (offset: 0.2 %) is equal to 210 MPa. The sample has a CCT geometry (Fig. 1a) and is subjected to cyclic tension with a load ratio R = 0.4. In the present analysis, only one loading/unloading history is considered after about 300,000 cycles for which the crack size $2a$ = 14.5 mm. First, a loading part is applied where the remote tensile stress is progressively increased to 147 MPa (leading to a theoretical mode I SIF K_I equal to 22.9 MPa$\sqrt{\text{m}}$ for a purely elastic behaviour) in 23 steps. In a second stage, the stress is decreased down to 0 MPa, in 7 steps. At the end of each step, a picture is taken by using a long distance microscope and a CCD camera (resolution: 1024 × 1280 pixels,

dynamic range: 12 bit) so that the physical size of one pixel is 2.08 µm. At this magnification, the raw surface is observed (Fig. 1b). Contrary to other materials (e.g., aluminium alloy [15]) no special surface preparation was used.

The displacement field is measured by using a Q4-DIC algorithm [21]. Therefore, a functional basis of bilinear functions for each component of the displacement field is sought over square elements (i.e., Q4P1-shape functions in the language of the finite element method [22]). Even though the displacement uncertainty is the lowest for large element sizes, the heterogeneity of the displacement prompts one to use small sizes [23]. To achieve a displacement uncertainty less than 2.5×10^{-2} pixel (or 52 nm), elements of size 12 × 12 pixels (or 623 μm^2) are used in this section. The latter is obtained by creating artificial images constructed from the true reference one (Fig. 1a) by using a sub-pixel translation in the range 0 to 1 pixel. (This is conveniently performed in Fourier space.) Then the correlation algorithm is applied to this pair of images, thus allowing for an evaluation of the standard displacement uncertainty. The average value over the studied interval defines the displacement uncertainty.

3.2 Analysis of the maximum load level

This preliminary study aims at choosing the relevant parameters to identify stress intensity factors. It is performed for the maximum load level of the cycle. Figure 2 shows a map of the two components of the displacement field, where the discontinuity of displacements appears clearly, mainly in mode I, although the crack does not propagate along the horizontal direction, had the experimental conditions been perfect. Consequently, an identification based on "perfect" boundary conditions, which is usually assumed by using finite element simulations, is not secure in the present case.

To identify the amplitudes ω_n and υ_n, a first approach is based on minimising displacements determined from the closed-form solution (7) compared to measured displacements $\mathbf{U}_{me}$ at N_{me} points $\mathbf{z}_{me}$, in the least squares sense

$$\Theta^2(\omega_n,\upsilon_n,\mathbf{z}_0,\varphi_0)=\sum_{me}\left\|\sum_n\left[\omega_n\mathbf{\Omega}_n\left\{(\mathbf{z}_{me}-\mathbf{z}_0)e^{i\varphi_0}\right\}+\upsilon_n\mathbf{Y}_n\left\{(\mathbf{z}_{me}-\mathbf{z}_0)e^{i\varphi_0}\right\}\right]-\mathbf{U}_{me}\right\|^2 \quad (16)$$

where $\|.\|$ is the classical norm 2. In the present case, N_{me} = 10788. The quantity $\mathbf{z}_0$ defines the location of the crack tip in the reference picture, and $-\varphi_0$ the angle of the crack face wrt. a reference direction in the picture. These last two parameters are critical to evaluate SIFs.

For each given location ($\mathbf{z}_0$, φ_0) of the crack, the values of the amplitudes, ω_n and υ_n, is computed by minimising Θ. The dimensionless residual error is measured as the ratio of the standard deviation of the displacement difference at convergence to that of the measured displacement. In the present case, there is no need to account for modes II (i.e., $\mathbf{Y}_1$ and $\mathbf{Y}_3$ are discarded) since the values of the stress intensity factor K_{II} is less than 3 % that in mode I and the influence on the identification error is vanishingly small. When $-3\le n\le 1$, $K_{\max}=18.5\,\text{MPa}\sqrt{\text{m}}$ and a residual error of 0.15 is found; when $-3\le n\le 2$, $K_{\max}=18.0\,\text{MPa}\sqrt{\text{m}}$ for a residual error of 0.13 and when $-3\le n\le 3$, $K_{\max}=20.6\,\text{MPa}\sqrt{\text{m}}$ with almost the same residual error (i.e., convergence is obtained). Since the residual error remains approximately identical, the 7 displacement fields are deemed sufficient to capture the crack kinematics in the present case. Figure 3 shows a map of the two components of the identified displacement field in very good agreement with the measured data (Fig. 2).

In the analysis of supersingular terms, the main emphasis is put on the first one, namely ω_{-1}. One defines the crack tip position such that $\omega_{-1}=0$ (see Section 2.5). Figure 4 shows that when the assumed crack tip position moves, the corresponding position r_1 also

moves and a quasi perfect proportionality (of slope −1) is observed between the two quantities when a ± 10 pixel variation is analyzed. This result validates the proposed definition of the crack tip position by using the first supersingular term.

In the previous analyses, all the measured data were considered, apart from an inner core of radius R_i equal to 35 pixels (or 73 μm) and points located at a distance d_i less than 12 pixels (or 25 μm) from the crack faces (these values were taken equal to element size *l* of the DIC procedure, since the elements are then traversed by the crack and the corresponding displacement evaluation is uncertain). Let us first define an outer radius R_o from the crack tip in which the measurement points are considered. Figure 5a shows the sensitivity of the value of the mode-I SIF on that of R_o for a fixed crack tip position. When $R_o < 1200$ pixels (or 2.5 mm), some of the points located far from the crack tip are not considered. When the 7 fields are considered and $R_o > 500$ pixels (or 1 mm), the value of $K_{\max}$ remains constant as well as the identification quality. Therefore, the number of chosen displacement fields is sufficient to identify the SIF value. In Fig. 5b, the change of the identified value of $K_{\max}$ is shown as a function of the inner radius R_i for the same crack tip position. As long as R_i remains less than 160 pixels (or 330 μm), the residual does not change significantly, while the variation of $K_{\max}$ is less than $\pm 0.2\ \mathrm{MPa}\sqrt{\mathrm{m}}$ (to be compared with a mean value of the order of $20.4\ \mathrm{MPa}\sqrt{\mathrm{m}}$). The minimum identification error is reached for an interpolated value equal to 75 pixels (or 160 μm). It is to be noted that the extent of the plastic zone size under cyclic loadings [4] reads

$$R_y = \frac{1}{\pi}\left[\frac{(1-R)K_{\max}}{2\sigma_y}\right]^2 \tag{17}$$

and is of the order of 340 μm (or 164 pixels) for the studied material when R = 0.4 and $K_{\max} = 22.9\ \text{MPa}\sqrt{\text{m}}$. Its effect on the identification appears clearly in Fig. 5b where the identification quality degrades for values of R_i greater than 180 pixels (or 370 μm).

From all the results obtained in this section, the following parameters are considered in the sequel. Seven displacement fields are chosen (i.e., $-3 \le n \le 3$). All the measurement points are used apart those such that $\Re(\mathbf{z}) < 0$ and $\Im(\mathbf{z}) < d_i = 12$ pixels (i.e., intersecting the crack faces), as well as $|\mathbf{z}| < R_i =$ 75 pixels (or 156 μm). The position $\mathbf{z}_0$ and the angle φ_0 are those determined for the maximum level (see Fig. 4). They will be kept constant for the whole cycle analysis. The parameter r_1 will enable for crack tip adjustments.

3.3 Analysis of a loading/unloading cycle

The sequence of 30 steps is now studied. Figure 6 shows the value of the SIF as a function of the applied load level P. Two regimes are observed. First, for small load levels (i.e., P < 6.5 kN), the value of the SIF is equal to zero (i.e., the crack remains closed). Second, above the value of 6.5 kN, there is a linear dependence of the SIF with the applied load. The dashed lines correspond to the following expression for the SIF K_I

$$K_I = Z \frac{\langle P - P_{op} \rangle}{bw^{1/2}} \tag{18}$$

where $P_{op} = 6.5$ kN, $b = 5$ mm, $w = 30$ mm, and $Z = 0.49$ a dimensionless parameter. The root mean square (RMS) error in terms of SIF between this expression and the raw measurements is less than $0.5\ \text{MPa}\sqrt{\text{m}}$.

The threshold P_{op} corresponds to the effect of small scale yielding. As first proposed by Elber [24,25], there exists a first regime for which, because of plastic flaw, the crack does not open. Beyond a critical value, the crack opens and there is linear relationship between the

applied load and the corresponding SIF. Instead of an effective SIF, one may rather consider an effective load level defined by $\langle P - P_{op} \rangle$. The so-called opening SIF K_{op} is thus expressed as

$$K_{op} = \frac{ZP_{op}}{bw^{1/2}} \tag{19}$$

and is estimated equal to $3.7 \pm 0.5 \text{MPa}\sqrt{\text{m}}$ (Fig. 6).

If plasticity is neglected, the SIF factor for a CCT sample reads

$$K_I = \frac{ZP}{bw^{1/2}} \tag{20}$$

where Z is a dimensionless parameter defined by [26]

$$Z = \left(\frac{\beta}{\cos\beta} \right)^{1/2} \left(0.707 - 0.007\beta^2 + 0.007\beta^4 \right) \quad \text{with} \quad \beta = \frac{\pi a}{2w} \tag{21}$$

In the present case, $Z = 0.45$. This value is to be compared with the parameter Z found equal to 0.49, i.e., with a 10 % difference compared with the theoretical value. This result validates the approach followed herein; in particular, the use of supersingular displacement fields.

Figure 7 shows the change of the offset parameter r_1 as a function of the applied load when the latter is greater than 15 kN. The higher the applied load, the smaller the offset. For values of the effective load greater than 75 % of the maximum value, the RMS variation of r_1 is of the order of 10 pixels (or 21 μm). This result shows that the location of the crack tip is determined within a 10-pixel standard uncertainty for the considered level range. As the effective load decreases, r_1 increases and the effective crack tip position moves away from its extreme position obtained for the maximum load level.

4. Integrated DIC

In the following, an alternative route is followed. It consists in using the displacements derived in Section 2.1 *directly* at the measurement stage. Therefore there is no

decoupling between the measurement and identification stages. It is referred to as integrated DIC (or I-DIC [16,23]). As for classical DIC, one considers a reference image, defined as f, e.g., a grey level distribution. An in-plane displacement field $\mathbf{u}(\mathbf{x})$ is defined. The passive advection of the texture f by the displacement field creates a "deformed image," g, such that

$$g(\mathbf{x}+\mathbf{u}) = f(\mathbf{x}) + \varepsilon(\mathbf{x}) \tag{22}$$

where $\varepsilon(\mathbf{x})$ is noise induced by image acquisition. In the following, it is assumed that the noise level, ε, is neglected either because of its low amplitude with respect to those of f and g, or because of its scale separation with significant components of the displacement field. Equation (22) is the integral form of the "optical flow conservation." The problem to address is the determination of the displacement field $\mathbf{u}$ from the exclusive knowledge of f and g. As such, the problem is ill-posed, unless additional assumptions are made on the regularity of the displacement field so that the information is sufficient to determine $\mathbf{u}$ with a reasonable accuracy [27].

4.1. General formulation

Let us introduce the following objective functional Φ operating on displacement fields $\mathbf{v}$

$$\Phi^2(\mathbf{v}) = \iint [g(\mathbf{x}+\mathbf{v}) - f(\mathbf{x})]^2 d\mathbf{x} \tag{23}$$

In the absence of noise, this functional reaches its minimum value, 0, for $\mathbf{v} = \mathbf{u}$ [see equation (22)]. The trial displacement $\mathbf{v}$ may be any choice. To fulfil a smoothness assumption on $\mathbf{u}$, $\mathbf{v}$ are either low-pass filtered or chosen in a subspace of suited functions. Let us first assume that f and g are sufficiently smooth at a small scale, and the displacement small enough in amplitude so that a Taylor expansion of g up to the first order is introduced in equation (23)

$$\Phi^2(\mathbf{v}) = \iint [g(\mathbf{x}) - f(\mathbf{x}) + \mathbf{v}(\mathbf{x}).\nabla g(\mathbf{x})]^2 d\mathbf{x} \tag{24}$$

Equation (24) corresponds to the objective functional associated with the *linearised* optical flow equation. The displacement field is decomposed as a linear combination of (chosen) basis functions $\boldsymbol{\eta}_j(\mathbf{x})$

$$\mathbf{v} = \sum_j \boldsymbol{\eta}_j(\mathbf{x}) v_j \tag{25}$$

so that Φ^2 becomes a quadratic form in the amplitudes v_j. The extremality condition thus dictates, for all j,

$$\left[\iint (\nabla g \otimes \nabla g)(\mathbf{x}) : (\boldsymbol{\eta}_j \otimes \boldsymbol{\eta}_k)(\mathbf{x}) d\mathbf{x}\right] \mathbf{v}_k = \iint [f(\mathbf{x}) - g(\mathbf{x})] \nabla g(\mathbf{x}) . \boldsymbol{\eta}_j(\mathbf{x}) d\mathbf{x} \tag{26}$$

where $\otimes$ denotes the dyadic product and ':' the contraction with respect to two indices. This system is written in a matrix form as

$$[\mathbf{M}]\{\mathbf{w}\} = \{\mathbf{m}\} \tag{27}$$

where $\{\mathbf{w}\}$ is a vector containing all the unknown components v_j, $[\mathbf{M}]$ and $\{\mathbf{m}\}$ are *known* quantities dependent upon f, g, and $\boldsymbol{\eta}$. One can note that the dyadic product $\nabla g \otimes \nabla g$ by itself cannot be inverted (it has always a zero eigenvalue in the direction normal to the gradient of g), and hence this formula cannot be used to determine v_j, if $\boldsymbol{\eta}_j$ tends to a Dirac distribution, as anticipated from the remark on the necessary regularity of $\mathbf{v}$. However, if the functions $\boldsymbol{\eta}_j$ are chosen to be restricted to wavelengths much greater than the correlation length of the texture, the left-hand side operator becomes a *genuine* definite positive operator.

4.2. Application to the analysis of a crack

The results derived in Section 4.1 allow us to propose an integrated approach to the measurement *and* the identification problems. By choosing *a priori* a basis of functions $\boldsymbol{\eta}_i(\mathbf{x})$ relevant to an experiment, the identification of the unknown amplitudes v_j not only provides information on the displacement features but also yields quantities to be identified from a

mechanical point of view. This type of technique was used to decompose the displacement field with linear functions, sines and cosines [28] for 1D signals. The same type of procedure was extended to 2D situations in which a spectral decomposition is assumed [29], to identify elastic parameters [23] or to measure stress intensity factors in brittle materials [16].

In the present case, the chosen basis consists of the eigenfunctions $\mathbf{\Omega}_n$ and $\mathbf{Y}_n$ (Section 2.1). The unknown amplitudes are then the components ω_n and υ_n. For each assumed crack tip position, the decomposition is performed, but more importantly, a global quality factor is obtained, and even a local map of non-resolved differences [equation (24)]. This feature is in turn utilised to identify the best location in the sense of lowest global error Φ. In the following, the seven displacement fields used in Sections 3.2 and 3.3 are also used in the present analysis.

4.3. Application to a loading/unloading cycle

The same type of analysis as in Section 3.3 is performed with the integrated approach. Only one element of size 512 × 512 pixels (or 1.13 mm^2) is used. All the pixels are used apart from those such that $\Re(\mathbf{z}) < 0$ and $\Im(\mathbf{z}) < d_i = 12$ pixels (to be consistent with the *a posteriori* analysis), as well as $|\mathbf{z}| < R_i = 75$ pixels (or 156 μm).

The detailed procedure to estimate the amplitude of the displacement field is quite similar to that presented in Ref. [12]. First, a gross determination of the displacement field is searched for using coarse-grained images, where superpixels are defined as averages of the true pixel values on squares of size $2^n \times 2^n$ pixels with $n = 3$ to start off with. After a first determination of the mean displacement, the strained image is corrected for using a linear interpolation. The process is repeated until convergence. Then a similar determination is carried out on a finer image where the coarse-graining is performed for $n = 2$, and similarly down to the original images. This provides a faster convergence, but more importantly, it

avoids spurious trapping into secondary minima when the displacement amplitude is large. Each determination at any scale is performed using the above formulation (26) for assembling the linear system. Small variants are however introduced to obtain a more robust and reliable scheme. The gradient of the image is computed over the average of the reference and strained image to symmetrise the problem. Those gradients are evaluated using an FFT routine. The latter provides us with a convenient tool to interpolate the image at subpixel resolution. However, FFT suffers from discontinuity effects at the boundary (it implicitly assumes periodic fields). To minimize this effect, an artificial treatment on the image is introduced by substituting the actual grey level values at each edge by the average of the left and right (or top and bottom) columns (resp., rows). This elementary modification reduces very significantly the spurious edge effects. Very few iterations at each scale are needed to achieve convergence.

First, the most likely crack tip position is determined by analyzing the maximum load level. A 25 pixel (or 52 μm) difference is observed when compared with that given by the *a posteriori* analysis. In the present case, the unresolved differences are measured in terms of grey levels [see equation (24)]. When the map of Φ is analysed and related to the dynamic range of the considered region of interest, a maximum value of the order of 1 % is obtained (Fig. 8). It follows that the displacement evaluation is deemed secure and the corresponding SIF value is trustworthy. Many unresolved differences are masked, in particular along the crack mouth. It can be noted that the remaining unresolved and unmasked differences are uncorrelated, thereby indicating that the basis of considered displacements is sufficient to describe the present experiment. Figure 9 shows the map of displacements for the highest load level. It is very close to those of Figs. 2 and 3.

The loading/unloading cycle of Section 3.3. is studied again. Figure 10 shows the result to be compared with Fig. 6 for the *a posteriori* analysis. The same general trends are

observed, namely, two distinct regimes are obtained. The opening load level P_{op} is here equal to 9 kN instead of 6.5 kN, and the dimensionless constant $Z = 0.45$. This value is in excellent agreement with Eqn. (21). The RMS difference between the measured SIFs and the approximation (18) is now about $0.6\,\mathrm{MPa}\sqrt{\mathrm{m}}$. The opening SIF is here estimated at $4.6 \pm 0.6\,\mathrm{MPa}\sqrt{\mathrm{m}}$. All these results (cross)validate the two approaches discussed herein.

5. Summary and perspectives

The analysis of crack displacement fields based on digital image correlation has been described in terms of a post-processing analysis, and an integrated approach. In both cases, the definition of a suited library of displacement field reveals a key ingredient to a precise and reliable evaluation of the crack geometry and stress intensity factor. When applied to a complete loading and unloading cycle, it is shown that a finite load is required to open the crack. Past this threshold, the stress intensity factor is a linear function of the load, with a proportionality that is consistent with a purely elastic behaviour. Moreover, no systematic increases of the residual error map are detected neither close nor remote to the crack tip, so that stress field inhomogeneity, or crack tip plasticity seem negligible within one loading cycle (taking place after a first load history of 300,000 cycles).

Let us also stress the interest of using the first supersingular elastic field in order to locate very precisely the equivalent crack tip position, as demonstrated by the consistent estimate of the actual crack tip position obtained for different initial trial values (Fig. 4). Furthermore, the integrated approach is also seen as yet another way of using the concept of "*diffuse stress gauging*" [30,23]. It refers to the fact that the support of the "stress" gauge is diffuse on the sample face. In that sense, it is a very good "*cracking gauge*" to measure stress intensity factors.

The methodology used in this paper is directly applicable to a broad class of different materials (brittle to ductile) and test geometries. This study illustrates the level of accuracy that is obtained on the stress intensity factor and crack geometry using a high quality long-distance microscope, but otherwise a quite common equipment. Let us underline for instance that the crack opening discontinuity at maximum load and at the most remote point of the crack tip is of order 10 μm.

It would be of interest to extend the analysis to more complex loading conditions so as to address for instance mixed mode crack loading, or the initial stage of fatigue where plastic yielding is more developed in comparison with the crack size. Investigating three dimensional fatigue cracks using X-ray tomography constitutes also a very challenging direction for future investigation.

Acknowledgements

This work was funded by the CETIM Foundation grant entitled PROPAVANFIS: "Advanced methods for the experimental and numerical analysis of crack propagations under complex loadings."

References

[1] Kanninen, M.F., Popelar, C.H. (1985) *Advanced Fracture Mechanics*. Oxford University Press, Oxford (UK).
[2] Beremin, F.M. (1983) A Local Criterion for Cleavage Fracture of a Nuclear Pressure Vessel Steel. *Metallurgical Transactions A* **14A**, 2277-2287.
[3] Wells, A.A. (1961) Unstable crack propagation in metals: cleavage and fast fracture. Proc. *Crack Propagation Symp.*, 210-230.
[4] Rice, J.R. (1967) Mechanics of crack tip deformation and extension by fatigue. In *Fatigue crack propagation, STP 415*, ASTM, Philadelphia (USA), 247–309.
[5] Rice, J.R. (1968) A Path Independent Integral and Approximate Analysis of Strain Concentrations by Notches and Cracks. *ASME J. Appl. Mech.* **35**, 379-386.
[6] Hutchinson, J.W. (1968) Singular Behavior at the End of a Tensile Crack in a Hardening Material. *J. Mech. Phys. Solids* **16**, 18-31.
[7] Rice, J.R., Rosengren, G.F. (1968) Plane strain deformation near a crack tip in a power-law hardening material. *J. Mech. Phys. Solids* **16**, 1-12.
[8] Rastogi, P.K. (Edt.) (2000) *Photomechanics*. Springer, Berlin (Germany).

[9] Sutton, M.A., McNeill, S.R., Helm, J.D., Chao, Y.J. (2000) Advances in Two-Dimensional and Three-Dimensional Computer Vision. In *Photomechanics*, Springer, Berlin (Germany), Topics in Appl. Phys.**,** **77**, 323-372.

[10] Chiang, F.P., Asundi, A. (1981) A white light speckle method applied to the determination of stress intensity factors and displacement field around a crack tip. *Eng. Fract. Mech.* **15**, 115-121.

[11] McNeill, S.R., Peters, W.H., Sutton, M.A. (1987) Estimation of stress intensity factor by digital image correlation. *Eng. Fract. Mech.* **28** (1), 101-112.

[12] Huntley, J.M., Field, J.E. (1989) Measurement of crack tip displacement field using laser speckle photography. *Eng. Fract. Mech.* **30** (6), 779-790.

[13] Réthoré, J., Gravouil, A., Morestin, F., Combescure, A. (2005) Estimation of mixed-mode stress intensity factors using digital image correlation and an interaction integral. *Int. J. Fract.* **132**, 65-79.

[14] Forquin, P., Rota, L., Charles, Y., Hild, F. (2004) A Method to Determine the Toughness Scatter of Brittle Materials. *Int. J. Fract.* **125** (1), 171-187.

[15] Sutton, M.A., Zhao, W., McNeill, S.R., Helm, J.D., Piascik, R.S., Riddel, W.T. (1999) Local crack closure measurements: Development of a measurement system using computer vision and a far-field microscope. In *Advances in fatigue crack closure measurement and analysis: second volume, STP 1343*, ASTM, 145-156.

[16] Hild, F., Roux, S. (2006) Measuring stress intensity factors with a camera: Integrated Digital Image Correlation (I-DIC). *C.R. Mecanique* **334**, 8-12. See also, Roux, S., Hild, F. (2006) Stress intensity factor measurements from digital image correlation: post-processing and integrated approaches. *Int. J. Fract.* **140**(1-4), 141-157.

[17] Riddel, W.T., Piascik, R.S., Sutton, M.A., Zhao, W., McNeill, S.R., Helm, J.D. (1999) Determining fatigue crack opening loads from near-crack-tip displacement measurements. In *Advances in fatigue crack closure measurement and analysis: second volume, STP 1343*, ASTM, 157-174.

[18] Irwin, G.R. (1957) Analysis of the Stresses and Strains near the End of a Crack Traversing a Plate. *ASME J. Appl. Mech.* **24**, 361-364.

[19] Muskhelishvili, N.I. (1953) *Some basic problems of the mathematical theory of elasticity*. P. Noordholl Ltd, Grönigen (Holland).

[20] Williams, M.L. (1957) On the stress distribution at the base of a stationary crack. *ASME J. Appl. Mech.* **24**, 109-114.

[21] Besnard, G., Hild, F., Roux, S. (2006) "Finite-element" displacement fields analysis from digital images: Application to Portevin-Le Châtelier bands. *Exp. Mech.* (in press).

[22] Zienkievicz, O.C., Taylor, R.L. (1989) *The Finite Element Method*. McGraw-Hill, London (UK).

[23] Hild, F., Roux, S. (2006) Digital image correlation: from measurement to identification of elastic properties - A review. *Strain* **42**, 69-80.

[24] Elber, W. (1970) Fatigue Crack Closure under Cyclic Tension. *Eng. Fract. Mech.* **2**, 37-45.

[25] Elber, W. (1971) The Significance of Fatigue Crack Closure. In *Damage Tolerance in Aircraft Structures*, ASTM, STP 486, Philadelphia, 230-242.

[26] AFNOR (1991) *Pratique des essais de vitesse de propagation de fissure en fatigue*. Standard A 03-404, AFNOR, Paris (France).

[27] Horn, B.K.P., Schunck, B.G. (1981) Determining optical flow. *Artificial Intelligence* **17**, 185-203.

[28] Roux, S., Hild, F., Berthaud, Y. (2002) Correlation Image Velocimetry: A Spectral Approach. *Appl. Optics* **41** (1), 108-115.

[29] Wagne, B., Roux, S., Hild, F. (2002) Spectral Approach to Displacement Evaluation From Image Analysis. *Eur. Phys. J. AP* **17**, 247-252.
[30] Roux, S., Hild, F., Pagano, S. (2005) A stress scale in full-field identification procedures: A diffuse stress gauge. *Eur. J. Mech. A/Solids* **24**, 442-451.

Figure captions

Figure 1: -a-Reference picture of the CCT test (12-bit digitisation, 1024×1280 pixel resolution). -b-CCT geometry.

Figure 2: Vertical (a) and horizontal (b) displacement fields expressed in pixels (1 pixel is equal to 2.08 μm) in a CCT experiment measured by using a Q4-procedure with an element size $l = 12$ pixels.

Figure 3: Vertical (a) and horizontal (b) displacement fields expressed in pixels (1 pixel is equal to 2.08 μm) in a CCT experiment identified by using 7 displacement fields ($-3 \le n \le 3$) when $d_i = l = 12$ pixels and $R_i = 35$ pixels.

Figure 4: Estimated offset r_1 vs. assumed crack tip position. A linear fit (dashed line) with a slope of -1 is also shown.

Figure 5: -a-Identified stress intensity factor and residual vs. outer radius R_o when $R_i = 35$ pixels. -b-Identified stress intensity factor and residual vs. inner radius R_i when $R_o = 1024$ pixels. The dashed lines correspond to a piece-wise linear interpolation. In both cases, 7 displacement fields are considered.

Figure 6: Identified stress intensity factor vs. applied load. The dashed lines correspond to the expression (18). The value of the opening SIF and load is depicted.

Figure 7: Offset position vs. applied load. The dashed lines correspond to a quadratic interpolation.

Figure 8: Map of the residuals in grey levels at convergence for the integrated approach with $l = 512$ pixels. The dynamic range of the region of interest is 3052 grey levels. The dashed lines depict the masked areas.

Figure 9: Vertical (a) and horizontal (b) displacement fields expressed in pixels (1 pixel is equal to 2.08 μm) measured by using an integrated approach with l = 512 pixels. The displacements are not plotted in the masked areas.

Figure 10: Measured stress intensity factor vs. applied load. The dashed lines correspond to the expression (18). The value of the opening SIF and load is shown.

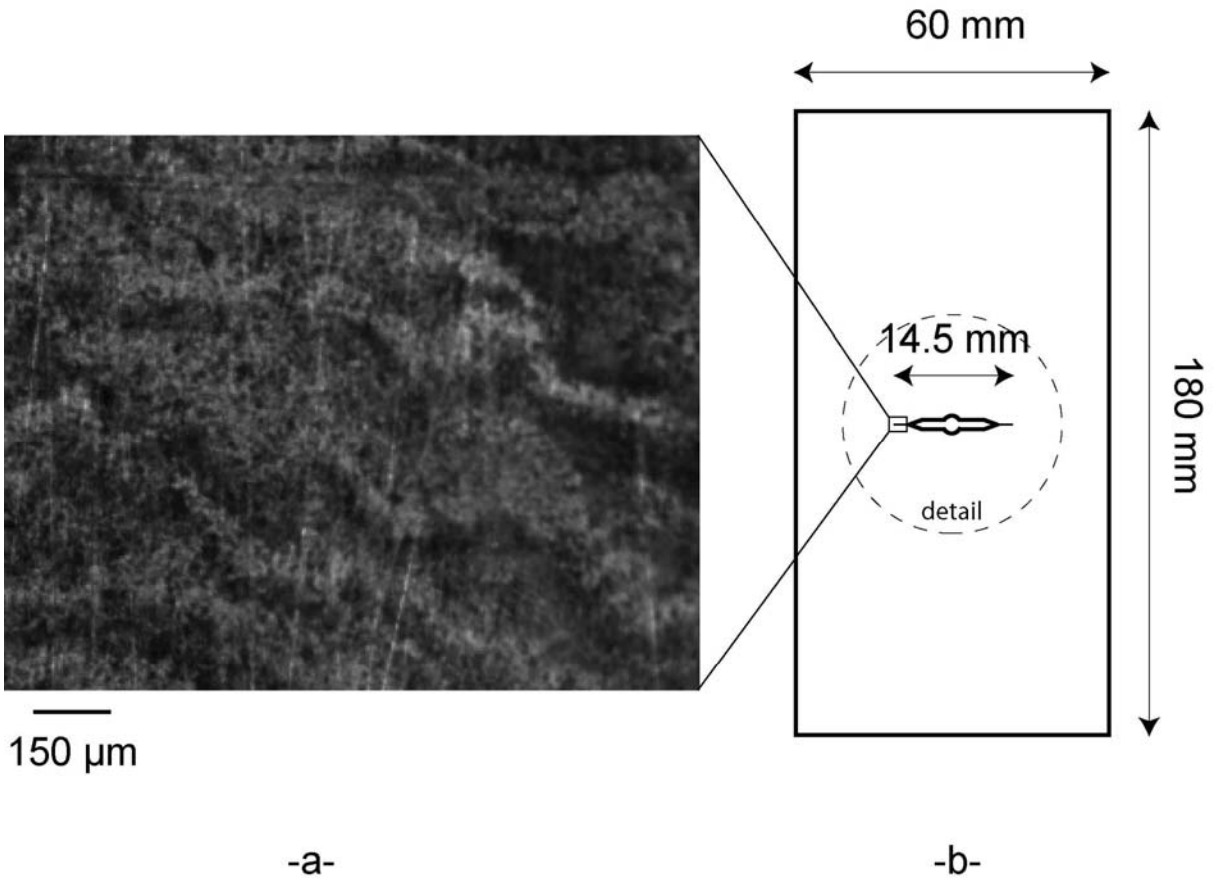

Figure 1

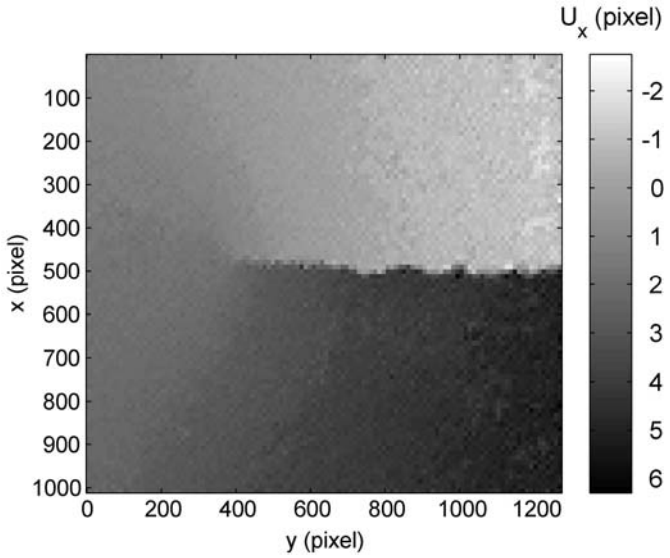
U_x (pixel)
x (pixel)
y (pixel)
100
200
300
400
500
600
700
800
900
1000
0
200
400
600
800
1000
1200
-2
-1
0
1
2
3
4
5
6

-a-

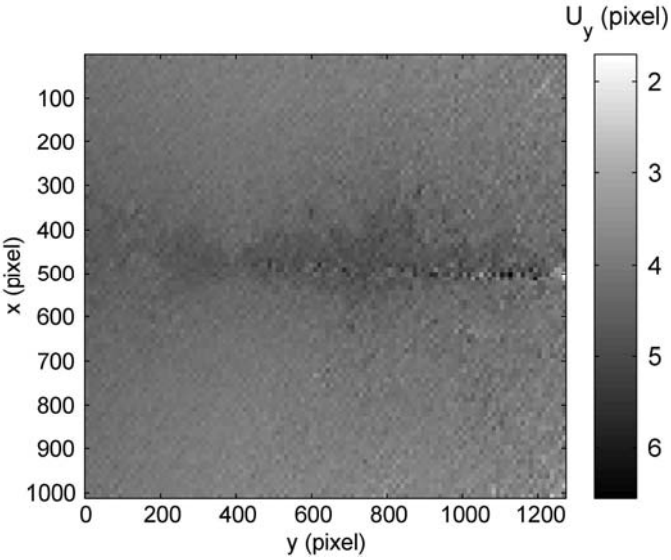
U_y (pixel)
x (pixel)
y (pixel)
100
200
300
400
500
600
700
800
900
1000
0
200
400
600
800
1000
1200
2
3
4
5
6

-b-

Figure 2

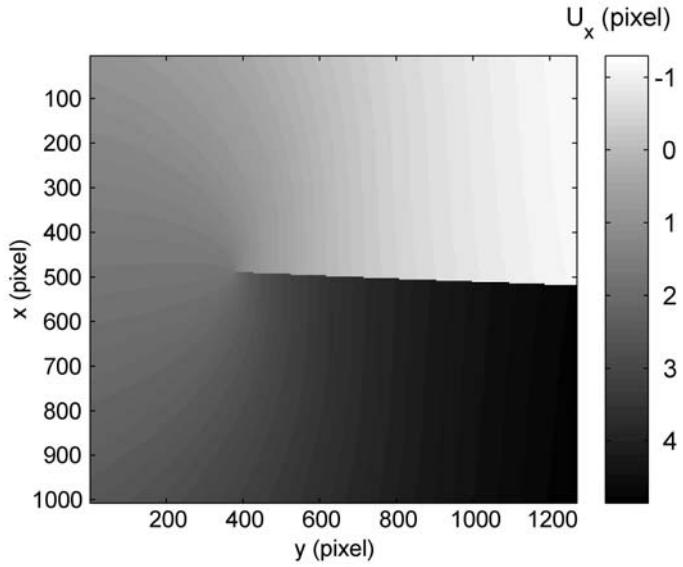
U_x (pixel)
-1
0
1
2
3
4
100
200
300
400
500
600
700
800
900
1000
x (pixel)
200
400
600
800
1000
1200
y (pixel)

-a-

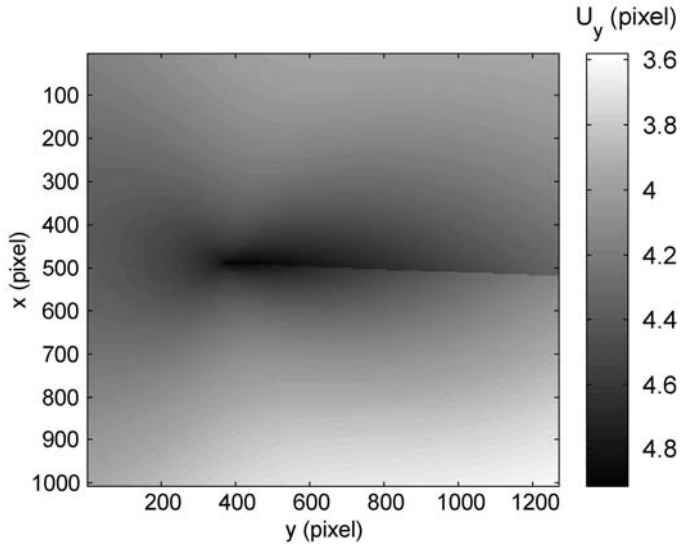
U_y (pixel)
3.6
3.8
4
4.2
4.4
4.6
4.8
100
200
300
400
500
600
700
800
900
1000
x (pixel)
200
400
600
800
1000
1200
y (pixel)

-b-

Figure 3

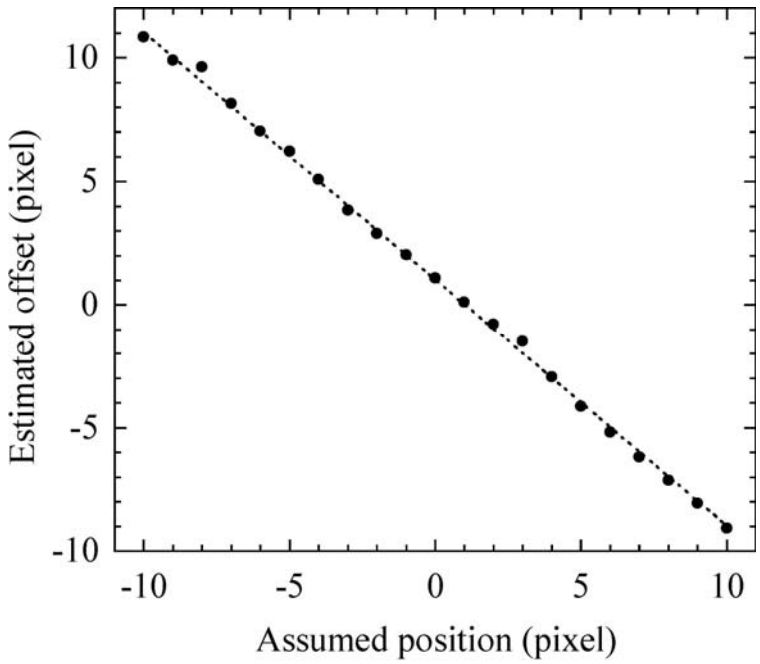
Estimated offset (pixel)
10
5
0
-5
-10
-10
-5
0
5
10
Assumed position (pixel)

Figure 4

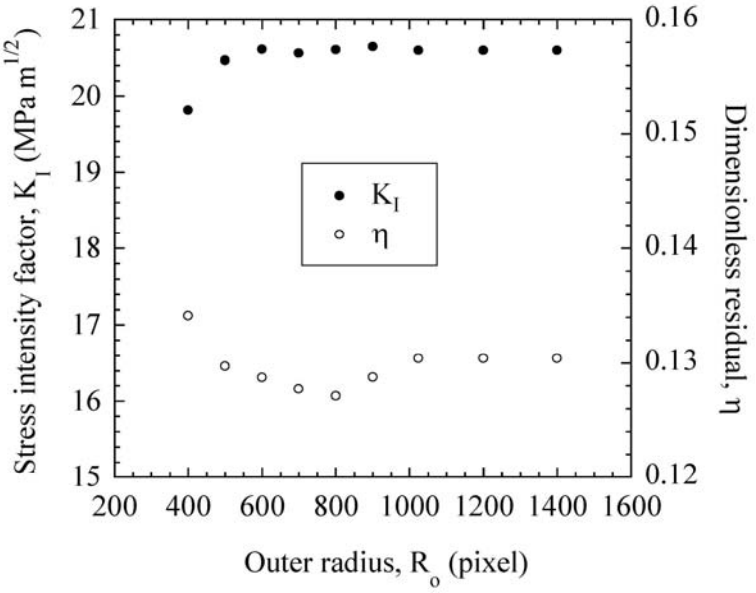
Stress intensity factor, K_I (MPa m$^{1/2}$)
Dimensionless residual, η
Outer radius, R_o (pixel)
K_I
η
21
20
19
18
17
16
15
0.16
0.15
0.14
0.13
0.12
200
400
600
800
1000
1200
1400
1600

-a-

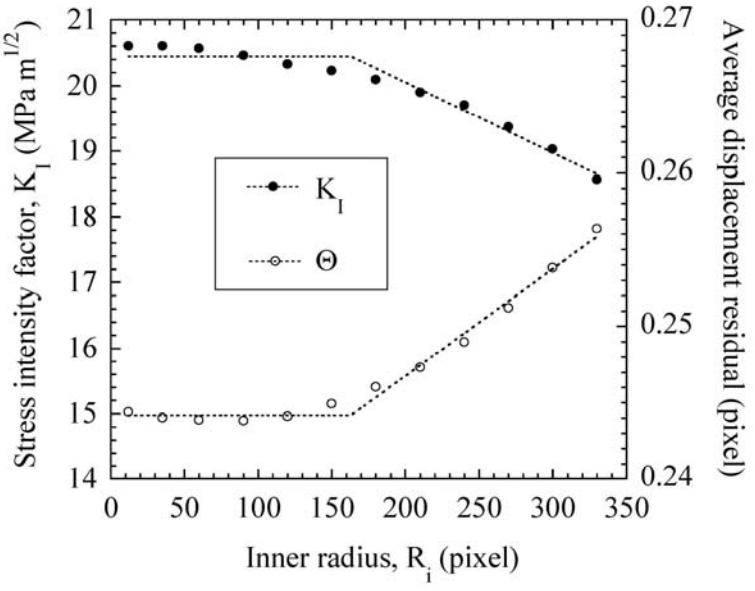
Stress intensity factor, K_I (MPa m$^{1/2}$)
Average displacement residual (pixel)
Inner radius, R_i (pixel)
K_I
Θ
21
20
19
18
17
16
15
14
0.27
0.26
0.25
0.24
0
50
100
150
200
250
300
350

-b-

Figure 5

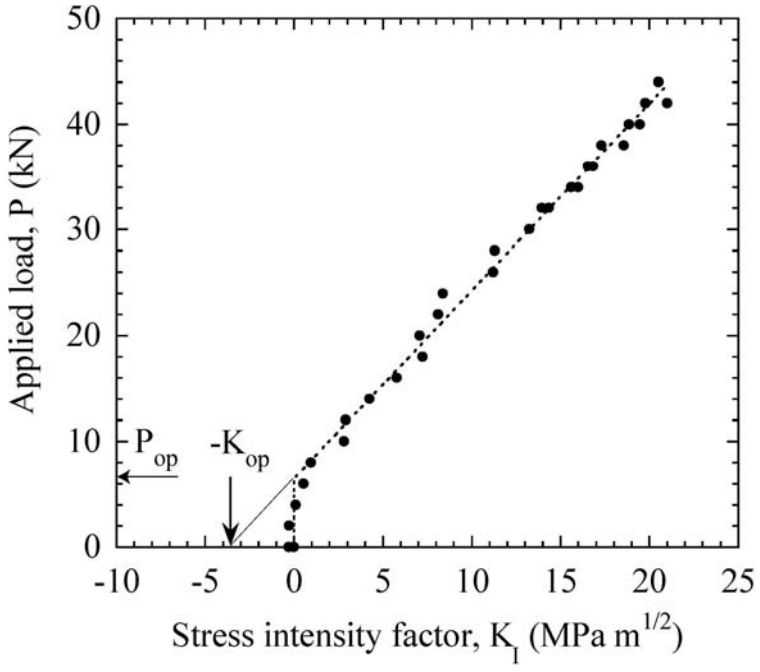
Applied load, P (kN)
Stress intensity factor, K_I (MPa m^1/2)
P_op
-K_op
50
40
30
20
10
0
-10
-5
0
5
10
15
20
25

Figure 6

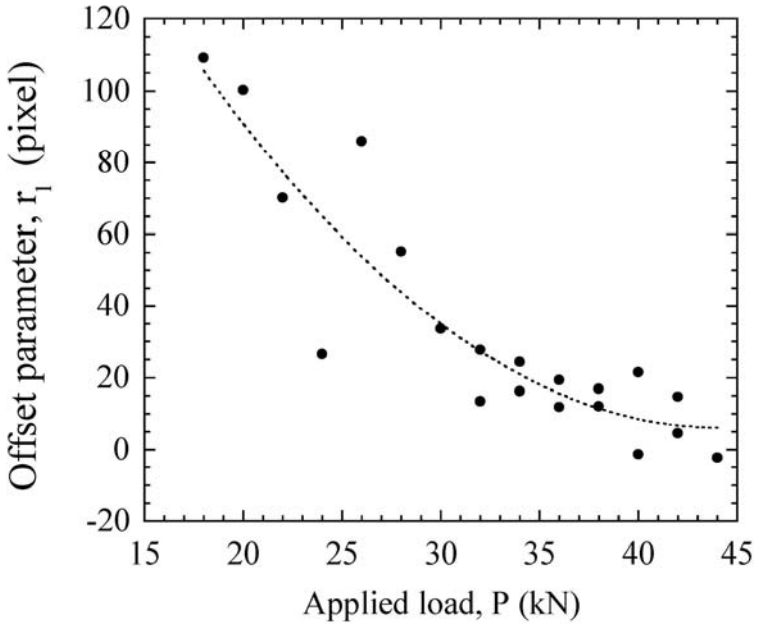
Offset parameter, r_1 (pixel)
120
100
80
60
40
20
0
-20
15
20
25
30
35
40
45
Applied load, P (kN)

Figure 7

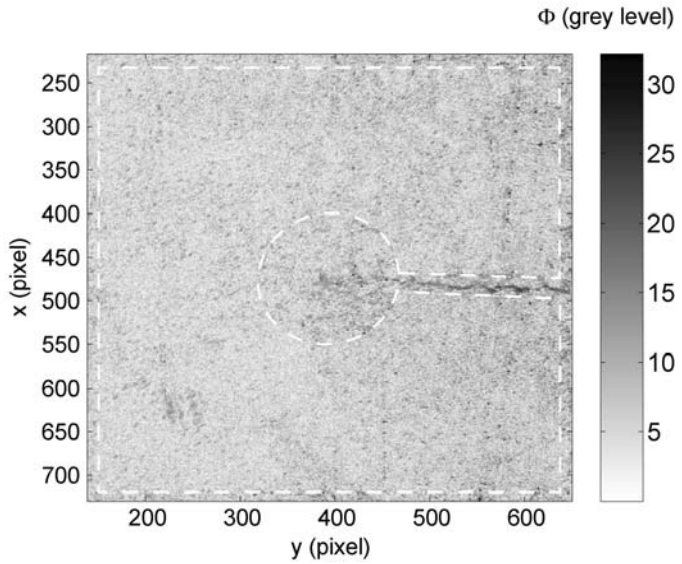
Φ (grey level)
x (pixel)
y (pixel)
250
300
350
400
450
500
550
600
650
700
200
300
400
500
600
30
25
20
15
10
5

Figure 8

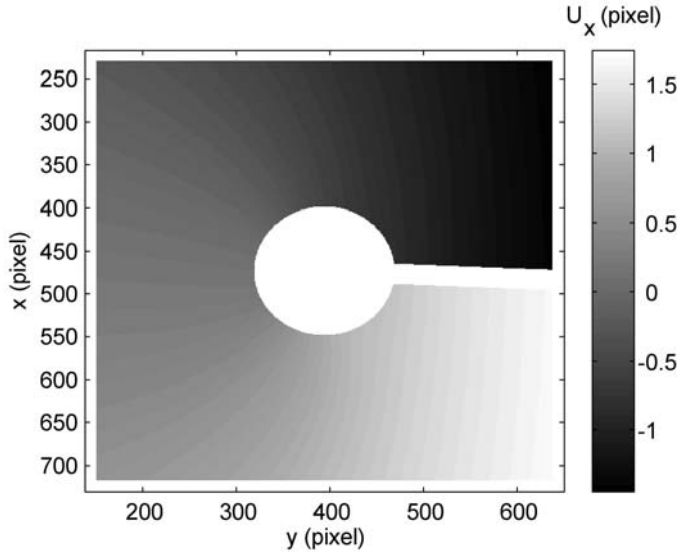
U_x (pixel)
x (pixel)
y (pixel)
250
300
350
400
450
500
550
600
650
700
200
300
400
500
600
1.5
1
0.5
0
-0.5
-1

-a-

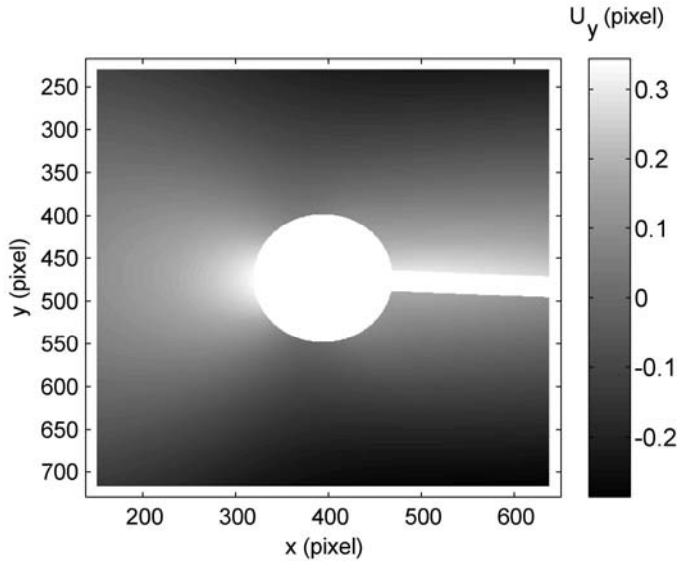
U_y (pixel)
y (pixel)
x (pixel)
250
300
350
400
450
500
550
600
650
700
200
300
400
500
600
0.3
0.2
0.1
0
-0.1
-0.2

-b-

Figure 9

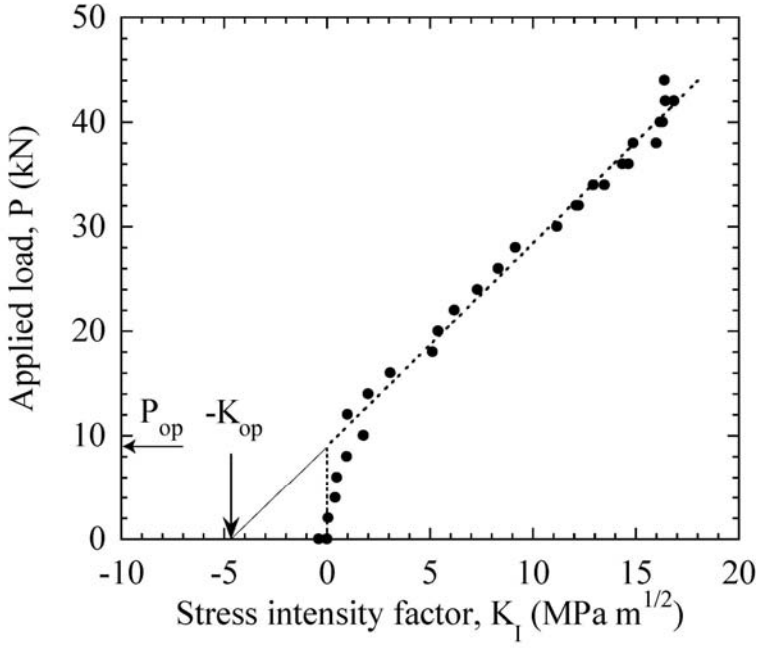
Applied load, P (kN)
Stress intensity factor, K_I (MPa m^1/2)
P_op
-K_op
50
40
30
20
10
0
-10
-5
0
5
10
15
20

Figure 10